Interconnected Graphene Networks with Uniform Geometry for Flexible Conductors

*Miao Xiao, Tao Kong, Wei Wang, Qin Song, Dong Zhang, Qinqin Ma, and Guosheng Cheng**

Controllable construction of graphene into specific architectures at macroscopic scales is crucial for practical applications of graphene. An approach of macroscopic and conductive interconnected graphene networks with controllable patterns, pore, and skeleton sizes via chemical vapor deposition is reported here. Specifically, the pore and skeleton sizes of 3D controllable graphene (3D-CG) architectures can be tuned from 10 to 50 μm and the orientation angles of building blocks can be designed as 45° and 90°. The electrical conductivity and density of 3D-CGs are measured at 60–80 S cm^{-1} and ≈3.6 mg cm^{-3}, respectively. The properties of 3D-CGs as flexible conductors and supercapacitor electrodes are reported, to explore the potential application in wearable devices and energy store.

1. Introduction

Graphene, a 2D monolayer of carbon atoms in a covalently bonded honeycomb arrangement, has attracted enormous research interests since its discovery by simple mechanical cleavage of graphite crystals.[1] Due to its unique structure, graphene possesses a lot of intriguing properties such as tremendous electron mobility,[2] remarkable thermal conductivity,[3] high surface area,[4] and excellent mechanical strength.[5] To integrate these promising properties into a practical system, one of the effective ways is to fabricate macroscopic 3D graphene architectures from individual graphene sheets.[6] Up to now, a number of 3D graphene architectures with different structures and various functions have been reported.[7] These novel materials not only preserve the structural merits and intrinsic properties inherited from graphene sheets, but also provide a high surface area, good electrical conductivity, porous structure, and strong operability,[8] making them widely applied in energy storage, catalysis,[10] and biomedicine.[11–13]

M. Xiao, Dr. T. Kong, Dr. W. Wang, Q. Song, D. Zhang, Q. Ma, Prof. G. Cheng
Key Laboratory of Nano-Bio Interface
Suzhou Institute of Nano-Tech and Nano-Bionics
Chinese Academy of Sciences
398 Ruoshui Road, Suzhou Industrial Park
Jiangsu 215123, P.R. China
E-mail: gscheng2006@sinano.ac.cn
M. Xiao, Prof. G. Cheng
University of Chinese Academy of Sciences
19A Yuquan Road, Beijing 100049, P.R. China

DOI: 10.1002/adfm.201502966

Recently lots of strategies have been utilized to construct 3D graphene architectures with specialized morphologies. Due to the great advance of single-crystal carbon architectures in nanoelectronics, a SiC wafer was used to grow designed 3D free standing single-crystal graphene by performing a simple single-step thermal process to meet the potential use in 3D electronic devices.[15] Because of low cost, high yield, easy scalability, and adjustability, the self-assembly of graphene oxide (GO), which is easily obtained by the oxidation of graphite, has been extensively developed for the fabrication of 3D graphene macroporous structures, such as graphene paper with great rigidity and strength,[16] honeycomb-like 3D graphene with superior electrical conductivity for supercapacitor application,[17] and transparent conductive fibers as conductive wire.[18] It is noted that these integrated 3D graphene structures present poor electric conductivity due to large structural defects in reduced graphene oxide (rGO) during the peeling and reduction, which limits their practical potentials. In order to obtain high quality 3D graphene with few defects, chemical vapor deposition (CVD) method is believed as an effective way using 3D porous metal as catalysts and templates, such as commercial Ni foams,[19] Ni nanowires,[20] templated Ni scaffold originated from polystyrene microspheres,[21] and Ni mesh.[22] After the CVD growth, free standing 3D graphene architectures can be acquired by etching of the porous metal catalysts. These 3D graphene architectures possess a monolithic interconnected structure with prominent electrical conductivity, compared to 3D graphene by self-assembly methods. However, the properties of 3D graphene are intensively related to their structures, more efficient controls of pore sizes and patterns of 3D graphene architectures are needed. Controllable fabrication of 3D graphene architectures with precise dimension and patterns not only manipulates the properties of 3D graphene to meet various demands, but also gives an access to interpret the functional mechanism of 3D graphene at different levels. Nevertheless, controllable fabricating of macroscopic, freestanding 3D graphene architectures has been rarely achieved.

In this work, we report a method for fabrication of macroscopic, freestanding 3D controllable graphene (3D-CG) architectures with well-defined patterns, pore, and skeleton sizes via CVD, using 3D Ni scaffolds with uniform patterns and sizes as sacrificial catalysts. Comparing to structures constructed by self-assembly and other CVD methods, the macroscopic 3D-CGs

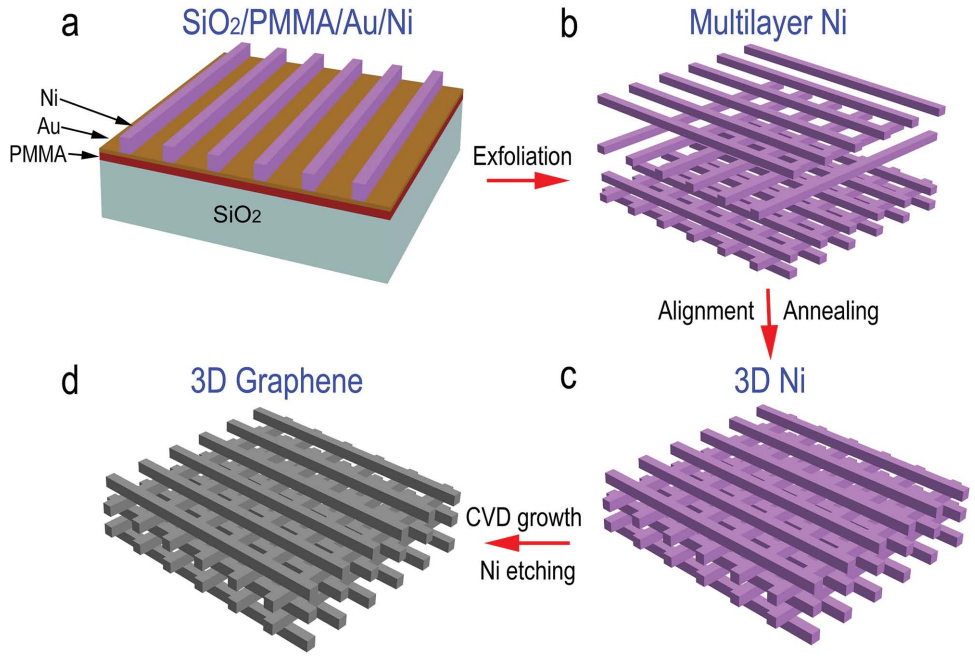

Scheme 1. Schematic illustration of the procedure used to fabricate a 3D-CG. a) Monolayer Ni skeletons fabricated based on semiconductor manufacturing technology. b) Multilayer Ni template aligned at 90°. c) 3D Ni template annealed at 700 °C with interconnected structure. d) A macroscopic, freestanding 3D-CG acquired using CVD method, followed by Ni etching process.

are of continuous and uniform interconnected structures with controlled patterns and sizes. Furthermore, the obtained 3D-CG sheets consist of fewer than ten stacked layers of carbon atoms with almost no defects. The electrical and mechanical properties based on 3D-CG/poly (dimethyl siloxane) composites as flexible conductors and 3D-CGs as supercapacitor electrodes were also investigated.

2. Results and Discussion

The overall experimental procedure for fabrication of 3D-CG is outlined in **Scheme 1**. Electroplating, which is convenient and economical to deposit large-area, thick metals, was utilized to construct 3D Ni scaffold. 200 nm thick polymethyl methacrylate (PMMA) film was first coated on SiO_2 substrate to separate monolayer Ni skeletons (Scheme 1a) from the substrate after photolithography. Monolayers were aligned at a certain degree to assemble designed multilayer Ni template (Scheme 1b). The Ni template was then annealed at 700 °C for bonding from each other to form an integrated 3D Ni scaffold (Scheme 1c). The 3D Ni scaffold was used as a template and catalyst for graphene growth in CVD system, where carbon atoms diffused into Ni by depositing CH_4 at 950 °C and subsequently precipitated as graphene on the Ni surface during cooling process.[23,24] To obtain free-standing 3D-CG, a thin layer of PMMA was deposited on the sample surface as a support to prevent the graphene network from collapsing during Ni etching by $FeCl_3$/HCl. After the PMMA layer was carefully removed by hot acetone, a macroscopic and freestanding 3D-CG was obtained (Scheme 1d). In this fabrication process, we can efficiently control the pore and skeleton size of 3D-CG by defining the photolithography mask and modifying the electroplating conditions. Additionally, we can also control the pattern of 3D-CG by aligning the multilayer Ni templates at certain degrees.

Generally, graphene can be readily fabricated based on Ni or Cu catalysts via CVD method. In this work, we first defined 3D Ni patterns with a controlled manner, thus the morphology and structures of prepared 3D-CGs follow the Ni templates, which allow to achieve a controllable fabricating of 3D graphene. Typical scanning electron microscopy (SEM) image of the Ni pattern after annealing at 700 °C is shown in **Figure 1**a. The regularly stacked Ni skeletons exhibit a highly interconnected structure with a thin surface oxidation layer (Figure 1b). After the CVD growth, Ni skeletons covered by graphene exhibited wrinkles and ripples structures (Figure 1c). The oxidation layer was totally removed by a reduction process (Figure 1d). Successful etching of Ni catalyst without any residual was confirmed by energy dispersive spectrometer (EDS) analysis after the etching (Figure 1f). Meanwhile, very tiny quantity of oxygen is probably induced during Ni wet etching.[22] The free-standing 3D-CG exhibits a highly regular pattern and size with a strong interconnected porous structure after the Ni etching (Figure 1e), although a small shrinkage of the graphene skeleton occurs. The 3D-CG inherits the interconnected 3D scaffold structure of the Ni template and all the graphene sheets in the 3D-CG are strongly connected from each other with no significant breaks and agglomeration.

The macroscopic, freestanding 3D-CGs are extremely light and flexible. **Figure 2**a shows an optical image of a four-layer skeleton of 3D-CG with 20 μm pore size and 40 μm skeleton size, possessing an ultralow density of ≈3.6 mg cm^{-3}. SEM image of Figure 2b indicates the sheet comprises hollow 3D-CG in a large-area, uniform, and well interconnected

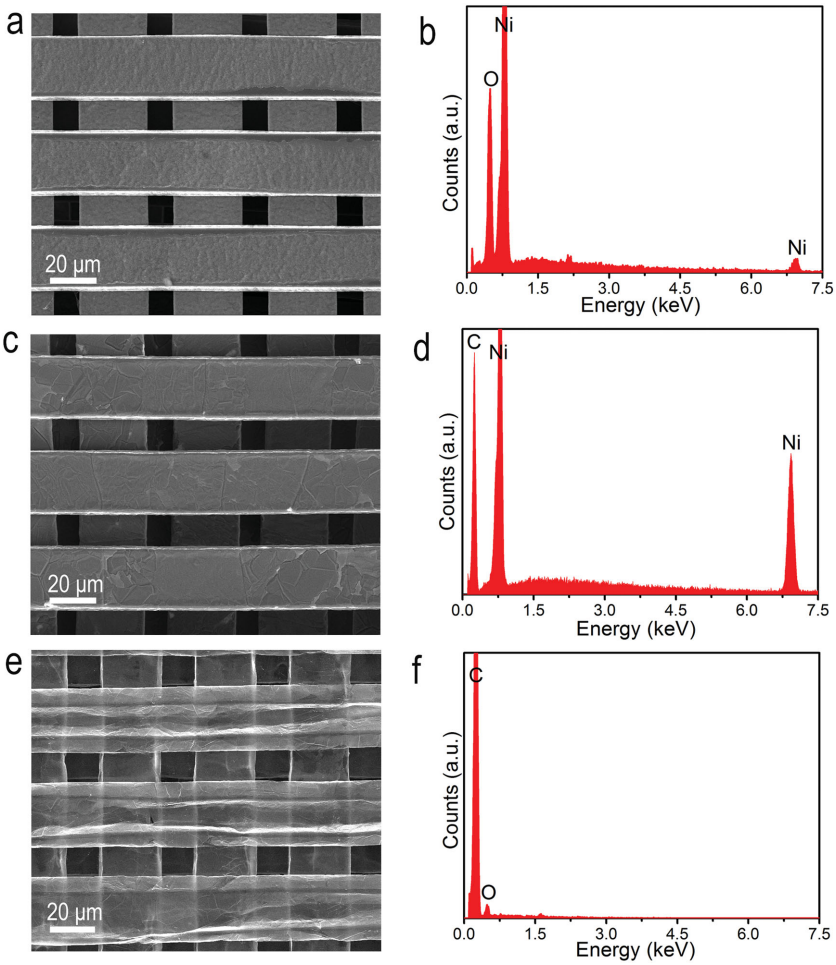

Figure 1. a) SEM images of the fabricated 3D Ni scaffold; c) 3D Ni covered by graphene after CVD; e) macroscopic, freestanding 3D-CG; and b,d,f) corresponding EDS spectra.

structures. Because of different thermal expansion coefficients of nickel and graphene, ripples and wrinkles were commonly exhibited on the graphene film[25] (Figure 2c). These wrinkles were proven to be positive on the differentiation of neural stem cells (NSCs) when 3D graphene foam (3D-GF) was used as the culture scaffold for NSCs.[11] Raman spectra (Figure 2d) acquired on 3D-CG present few-layer graphene features, which can be identified as three characteristic peaks, including a D peak at ≈1348 cm^{-1} associated with sp^3-hybridized carbon, showing defects or impurities in carbon materials; a G peak at ≈1580 cm^{-1} resulted from the E_{2g} vibrational mode of sp^2 carbon; and a 2D peak at ≈2704 cm^{-1} generated from the scattering of phonons at the zone boundary. The micro-Raman spectra illuminates a strongly suppressed defect-related D band, indicating overall high quality of the graphene in 3D-CG. We can also find that the number of graphene layers is different in various domains, which is attributed to the polycrystalline nature of the nickel scaffold, in which individual nickel grains may independently affect the thickness of the graphene film during CVD.[23] High-resolution transmission electron microscopy (TEM) micrographs (Figure 2e) show that the 3D-CG consists of few layers (less than ten) graphene, which is consistent with the Raman spectra. Most noteworthy are the graphene-ended square shape (Figure 2f), which can be effortlessly opened via mechanically cutting the ends of the graphene/Ni scaffold prior the Ni etching. Therefore, square, hollow 3D-CG with characteristic size is clearly present.

The fabrication process enables us to precisely modify the microstructure of 3D-CGs. The pore and skeleton sizes of 3D-CGs can be controlled by defining the mask and changing the electroplating conditions. We can further precisely control the pattern of 3D-CGs by aligning the multilayer Ni templates at certain degrees. For example, **Figure 3** depicts SEM images of four kinds of 3D-CGs, in which Figure 3a,c shows two different 3D-CGs designed by a mask with 25 μm pore size, 5 μm skeleton size and aligned the multilayer Ni scaffolds with 90° and 45°, respectively. Figure 3b,d shows two 3D-CGs designed by a mask with 20 μm pore size, 40 μm skeleton size and aligned the multilayer Ni scaffolds with 90° and 45°, respectively. The well-defined patterns and well-connected skeletons are observed. It is evident that by utilizing Ni scaffold with controllable size, a new type of 3D graphene with well-defined and predetermined dimensions has been fabricated, consequently providing key materials for advanced technology of controlled preparation of carbon materials from nanoscopic to macroscopic scales.

Elastic conductors and electric circuits are highly desirable for applications in flexible displays, smart clothing, and actuators.[27] Porous structure of 3D-CGs provides a great potential of retaining high conductivity of interconnects under substantial degrees of bending, twisting, and stretching deformation to meet the demand of flexible electric applications. To address those points, we fabricated 3D-CG/Polydimethylsiloxane (PDMS) composites by infiltrating 3D-CG with PDMS polymer. The electrical resistance testing results of the samples before and after PDMS infiltration presented no difference. Additionally, our 3D-CG/PDMS composites show a higher electrical conductivity of 60–80 S cm^{-1} with different pore and skeleton sizes of 3D-CGs, compared with that of previously reported 3D graphene grown via CVD.

Stretching effects on the resistance variation of the flexible composite conductors were investigated by testing the resistance change of the flexible composite conductors with two, six, and ten skeleton layers under different stretching ratios from 5% to 40% (**Figure 4**a). Higher resistance variations occur with an increasing degree of stretching. Meanwhile, the smaller number of skeleton layers results in the higher resistance variation that occurs under the same stretching ratios. The measured resistance change of flexible composite conductors with six skeleton layers tends to increase gradually from 15% to 150% as the extent of stretching increases

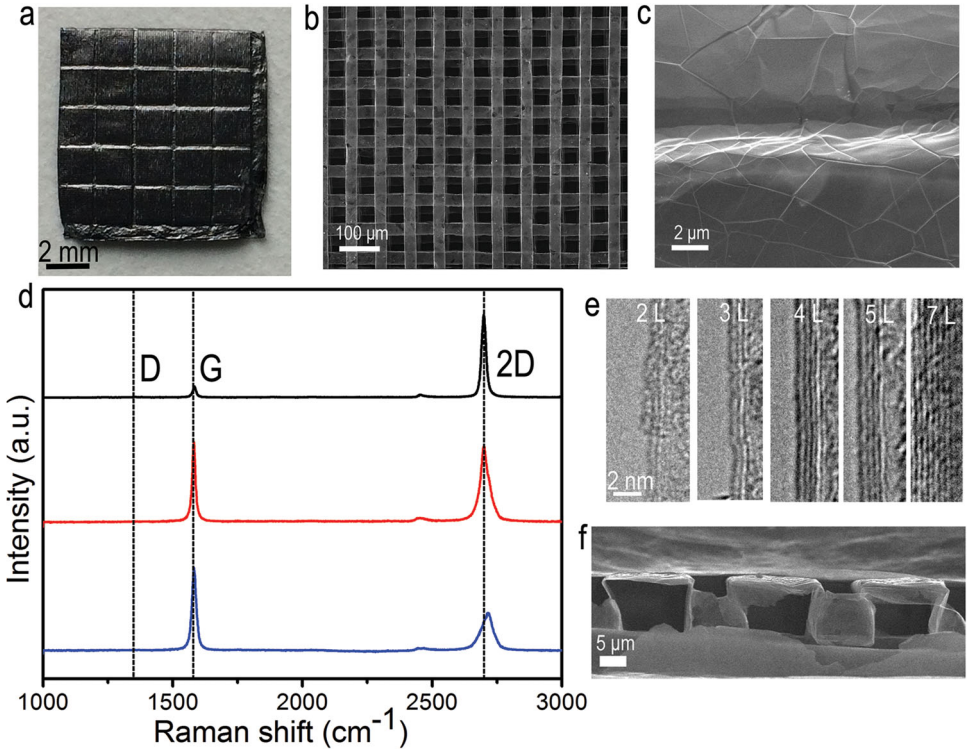

Figure 2. Morphological and structural characterizations of 3D-CGs. a) Photograph of a typical macroscopic, freestanding 3D-CG with ten-layer skeletons. b) SEM image of 3D-CG. c) Enlarged higher-magnification SEM image of 3D-CG. d) Typical Raman spectra acquired on the 3D-CG surface at different positions. e) HRTEM image on the wall edges of the 3D-CG. f) SEM image of the cross-section of the 3D-CG.

up to a maximum of 40%; on the contrary, 8%–56% for ten skeleton layers, which is much lower than that of six skeleton layers. Furthermore, the measured resistance of flexible composite conductors with two skeleton layers surpassed the measuring range, which might have broken the structure of the 3D-CG. Thus, the more number of skeletons layers, the less change of the resistance of flexible conductor and less the structure destruction during the mechanical deformation. The recovery of the resistance of the 3D-CG/PDMS flexible composite electrodes with six skeleton layers was also investigated, with degrees of stretching of 10%, 20%, 30%, as shown in Figure 4c. The change of resistance indicates a gradual increase as the stretching ratio increases from 10% to 30%, which is consistent to the behavior shown in Figure 4a. Once the stretched electrode is released, the initial resistance is recovered due to the high density of its interconnected graphene architecture.

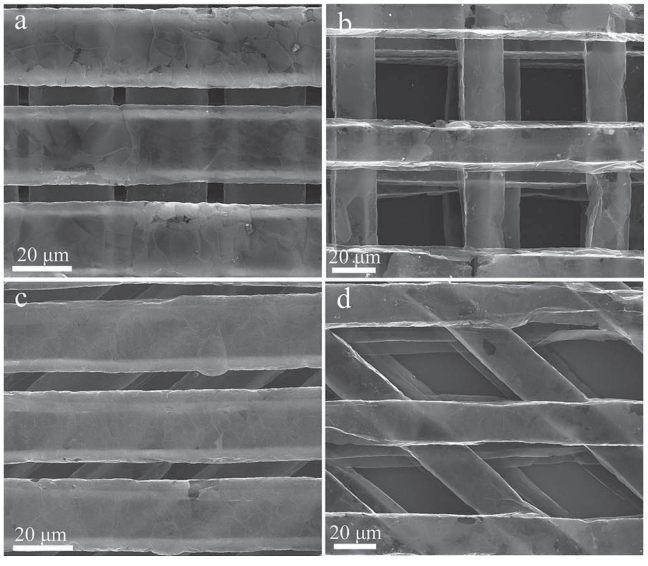

Figure 3. SEM images of 4 layer freestanding 3D-CGs with different patterns, pore, and skeleton sizes. a) 90° angle, 25 μm pore size, and 5 μm skeleton size. b) 90° angle, 20 μm pore size, and 40 μm skeleton size. c) 45° angle, 25 μm pore size, and 5 μm skeleton size. d) 45° angle, 20 μm pore size, and 40 μm skeleton size.

Furthermore, bending test was carried out using various radii of curvature fixed to the sample. The results in Figure 4b are similar with those of stretching tests. The measured resistance change of flexible composite electrodes with six skeleton layers increased gradually to 45% at a bending radius of 1.5 mm, but the resistance change for ten skeleton layers is 13.5%, which is much lower than that of six skeleton layers. This bending stability was constant throughout repeated tests at a bending radius of 3.5 mm, as shown in Figure 4d, where an average increase of 43% was observed and the resistance was well recovered when the degree of bending was relaxed after ten cycles. These results indicate the great potential of 3D-CG/PDMS composites for high-performance elastic conductors.

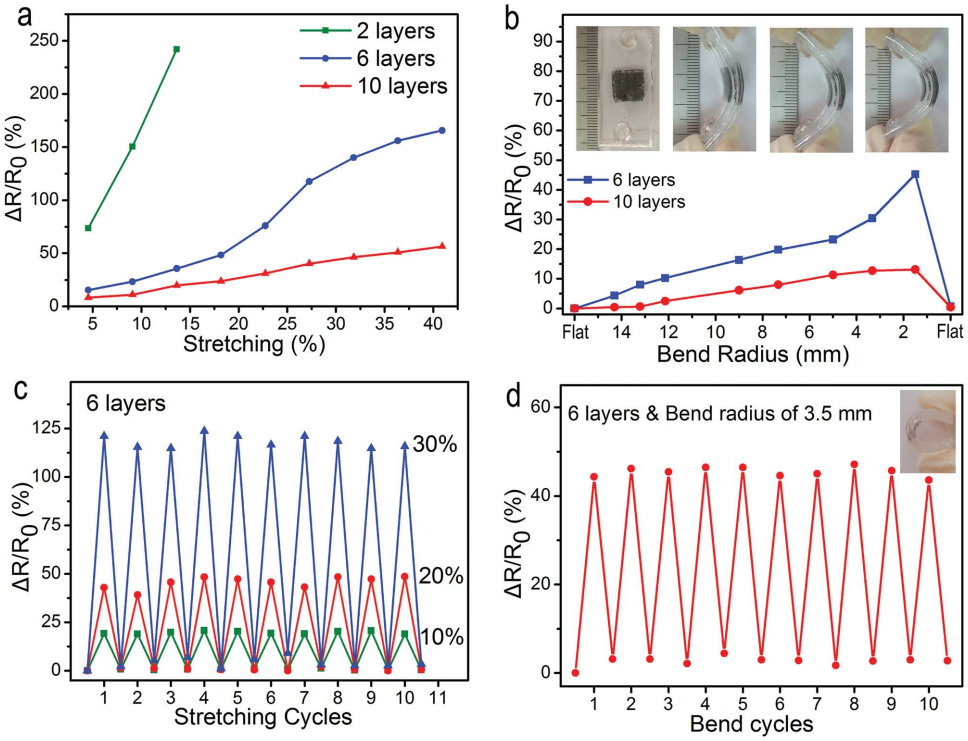

Figure 4. Resistance changes of 3D-CG/PDMS composite conductors under different mechanical deformation. a) Resistance change versus stretching of three composite conductors with different skeleton layers. b) Resistance variation of two composite conductors with different skeleton layers as a function of bending radius. c) Resistance variation of a six-layer skeleton 3D-CG/PDMS composite conductor depending on the stretching cycles. d) Resistance variation of a six-layer skeleton 3D-CG/PDMS composite conductor depending on the bending and recovery at a bending radius of 3.5 mm for 10 cycles.

In order to assess the utilization potential of 3D-CGs as supercapacitor electrodes, we investigated their electrochemical performance and compared them with the 3D-GFs. We chose a 3D-GF and a 3D-CG with four skeleton layers, 20 μm pore size and 40 μm skeleton size as the electrodes in electrical double-layer capacitors (EDLCs). Electrical connection to the foams is made via Cu wire attached with silver paste, which is coated with a nonconducting resin to prevent contact with the electrolyte. Three-electrode testing (Pt counter and Ag/AgCl reference electrodes) is performed in an aqueous 0.5 M Na_2SO_4 electrolyte. CV curves at a variety of scan rates are performed on all fabricated foams. The CVs retain a nearly symmetrical rectangular shape within a range of scan rates employed, which is characteristic of electrochemical double-layer capacitive behavior (**Figure 5**a). Galvanostatic charge–discharge plots (Figure 5c) show similar results; a pseudolinear discharge curve is apparent with slight nonlinearity apparent at similar potentials as the features seen in CV. Moreover, the current density of 3D-CG is much higher than that of 3D-GF, at the same scan rate of 2000 mV s^{-1} (Figure 5b).

To reveal the relationship between the specific areal capacitance and number of skeleton layers, we chose 3D-CGs with 20 μm pore size and 40 μm skeleton size and three different number of skeleton layers as the electrodes in EDLCs. The specific capacitance of the foam can be calculated using

$$C=\frac{I}{\Delta V/\Delta t S_{\text{proj}}} \tag{1}$$

Where C is the specific areal capacitance, I is the average discharge current, $\Delta V/\Delta t$ is the average potential sweep rate during discharge, and S_{proj} is the projected area of the sample. For a simple geometric consideration, the specific surface area per projected area, S_A, of a close packed array of hollow cuboid can be calculated using

$$S_A=\frac{2\left[nN(2x\alpha+2t\alpha)-2(n-1)N^2x^2\right]}{S_{\text{proj}}} \tag{2}$$

Where n is the number of layers of skeletons, x is the width of skeleton, y is the width of pore between skeletons, t is the thickness of skeleton, N is the number of skeletons per layer in the projected area, α is the side length of the square electrode. The first factor "2" is present to account for both the inside and outside surfaces of the cuboid. We assume the number of skeletons and pores are the same

$$S_{\text{proj}}=\alpha\times\alpha \tag{3}$$

$$\alpha=N(x+y) \tag{4}$$

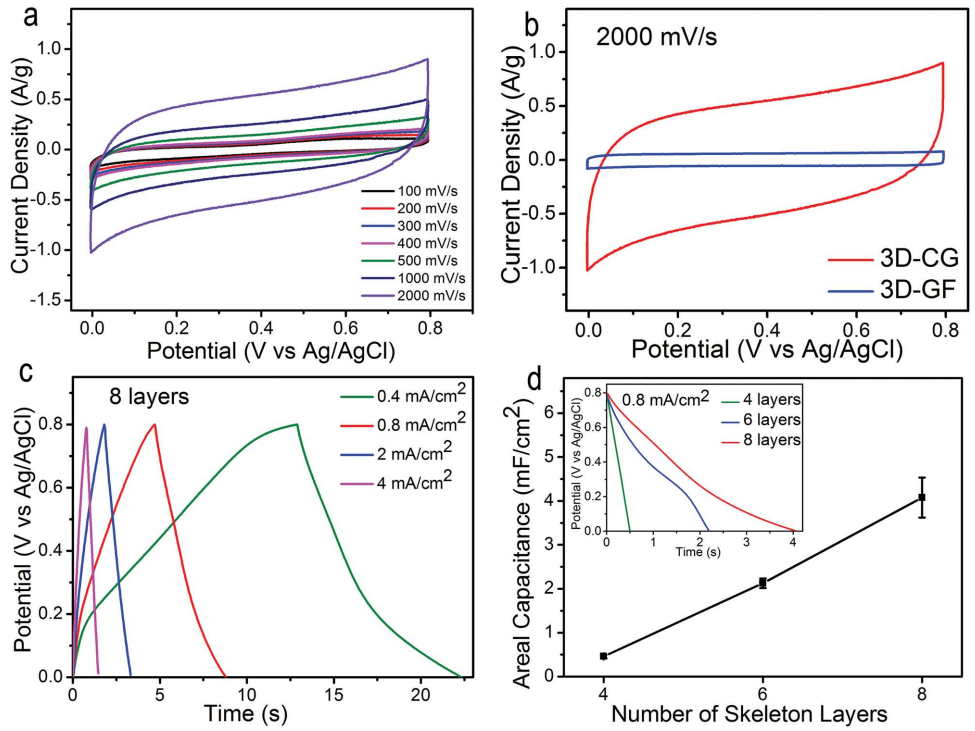

Figure 5. Electrochemical performance of 3D-CGs. a) CV curves of a 3D-CG in 0.5 M Na_2SO_4 solution from 100 to 2000 mV s^{-1}. b) CV curves compared between 3D-CG and 3D-GF at 2000 mV s^{-1}. c) Galvanostatic charge–discharge plots of a 3D-CG with eight layers of skeletons in 0.5 M Na_2SO_4 solution at various current densities from 0.4 to 4 mA cm^2. d) Calculated areal capacitance of three samples from discharge date. Inset shows discharge plots of three different numbers of skeleton layer at the same current densities of 0.8 mA cm^{-2}.

Combing Equations (2), (3), and (4) yields

$$S_A = 4n\left[\frac{x+t}{x+y} - \frac{x^2}{(x+y)^2}\right] + 4\frac{x^2}{(x+y)^2} \quad (5)$$

revealing that for the specific pore and skeleton size, the specific surface area per projected area (S_A), and hence the specific areal capacitance is expected to increase linearly with the number of layers, which is in a great agreement of experimental measurements (Figure 5d). Consequently, it is safe to conclude the macroscopic 3D-CGs has great potential in free-standing, flexible supercapacitor electrodes, which would also provide an ideal support for active materials, such as MnO_2,[28] Ni_3S_2,[29] NiO.[30]

3. Conclusion

In summary, we have developed a template-assistant CVD technique for a controllable fabrication of highly conductive interconnected graphene networks with precise pattern and dimension. The graphene sheets in the 3D-CG are seamlessly interconnected into uniform 3D flexible network with controlled pattern and skeleton size, which results into outstanding mechanical stability, ultralight, excellent electrical conductivity, and superior electrochemical performance. These properties show great promise for exploring new functions and advanced applications in high-performance electrically conductive polymer composites, elastic and flexible conductors for portable electronics and wearable sensors, electrode materials for high-performance supercapacitors.

4. Experimental Section

Fabrication Processes of Ni Scaffolds: The fabrication of Ni scaffolds follows a typical top-down microfabrication strategy. First, 200 nm thick PMMA layer was spin coated on a precleaned silicon dioxide (SiO_2) substrate, followed by 150 nm thick Au film deposition via magnetron sputtering (FHR Anlagenbau GmbH, Germany). AZ 4620 photoresist (AZ Electronic Materials, USA) was further spin-coated on the Au film with a spin rate of 1200 rpm for 40 s, followed by 180 °C prebake for 3 min. Afterwards, MA6/BA6 aligner (Süss Microtech, Germany) was utilized to expose the line patterns under hard mode. The exposure time was set as 45 s to obtain the designed feature sizes. After development, the substrate was immersed into an electroplating bath for Ni deposition. The thickness of Ni skeletons can be effectively controlled by sophisticated adjusting of the electroplating currents and time. The as-fabricated monolayer of Ni skeletons was then peeled off from the substrate after dipping in acetone for 12 h. Subsequently, we stacked and aligned —two to ten monolayers of Ni skeletons with specific angles and annealed at 700 °C for 3 min in a muffle furnace (TM-0912P, China) to bond the monolayers together. After naturally cooled down to room temperature, 3D Ni scaffolds with controllable patterns, pore, and skeleton sizes can be obtained.

Fabrication of Free-Standing 3D-CGs: The 3D-CGs were fabricated via CVD in a horizontal tube furnace (Thermcraft, USA). The as-prepared

3D Ni scaffolds were cut into 1 × 1 cm pieces and placed in a 1 in. -diameter quartz tube which was premounted in the furnace. The Ni scaffolds were first annealed at 950 °C for 10 min under H_2 (100 sccm) and Ar (100 sccm) atmosphere to clean their surface and eliminate surface oxidation layers. Next, 50 sccm of H_2 and CH_4 was introduced into the CVD system for 60 min, followed by cooled down to room temperature to allow graphene growth on the Ni scaffold surfaces. For comparison, 3D-GFs on commercial Ni foams (PPI 100 ± 10, Alantum Advanced Technology Materials, China) were prepared with identical conditions. To prevent structural collapse of 3D-CGs and 3D-GFs after the Ni etching process, the as-fabricated samples were first immersed in 4% PMMA for 2 h, followed by drying overnight at room temperature in a fume hood. This allowed a thin PMMA film to deposit between the pores and on the surfaces of the as-fabricated graphene/Ni scaffolds. The samples were then submerged into a $FeCl_3$ (1 M) solution for 48 h to chemically etch Ni from the scaffolds. The acquired 3D-CGs/PMMA and 3D-GFs/PMMA composites were sequentially rinsed with 1, 0.1, and 0.01 M HCl solutions, followed by rinsing with deionized water for 48 h to remove residual etching agents. Finally, PMMA film was dissolved in acetone at 60 °C to obtain clean 3D-CGs with controlled patterns and sizes and 3D-GFs.

Morphological and Microstructural Characterizations: The morphological and microstructural characterizations of the 3D-CG samples were investigated by field-emission SEM equipped with EDS (Quanta 400 FEG, FEI, USA). The crystallinity and number of the layer presented within graphene were examined by Raman spectrometer (LabRAMHR800, HORIBA, France) and TEM (Tecnai G2 F20 S-TWIN). For TEM observations, 3D-CG sheets were ultrasonically dispersed in ethanol for 45 min and then dropped onto a copper grid. The edges of the graphene films tend to fold back, thus allowing for a cross-sectional view and consequently determining the number of layers of the film.[31]

Electrical and Mechanical Characterization: In order to explore the flexible electrode application of 3D-CGs, PDMS was used to fabricate electrodes. Prior to infiltration with PDMS, a copper wire was connected to 3D-CG using conductive silver paste, which enabled efficient and reliable electric contact between copper wire and 3D-CG. The electrical and mechanical tests were carried out by measuring the electric resistance changes of 3D-CG/PDMS composite flexible conductors for deformation processes (stretching and bending). Stretching and bending effects on the resistance variation of the flexible composite conductors were carried out to test the relationship between mechanical deformation and electrical stability.

Supercapacitor Characterization: For the supercapacitor application investigation, three-electrode setup was utilized with a electrochemical workstation (CHI760E, Chenhua Instrument Co. Ltd., China), in which the macroscopic, freestanding 3D-CGs and 3D-GFs were used directly as work electrodes, a platinum wire as counter electrode and Ag/AgCl (3 M KCl) as reference electrode. 0.5 M Na_2SO_4 solution was used as electrolyte. Cyclic voltammetry (CV) scans were performed with a potential range from 100 to 2000 mV s^{-1}.

Acknowledgements

This work was financially supported by the Ministry of Science and Technology of China (MOST) (973 Grant number: 2014CB965003) and National Natural Science Foundation of China (NSFC) (Grant number: 51361130033). The authors are grateful for the professional services of Platforms of Characterization & Test and Nanofabrication Facility and Nano Fabrication Facility at Suzhou Institute of Nano-Tech and Nano-Bionics, Chinese Academy of Sciences.

Received: July 17, 2015
Revised: August 7, 2015
Published online: September 15, 2015

[1] K. S. Novoselov, A. K. Geim, S. V. Morozov, D. Jiang, Y. Zhang, S. V. Dubonos, I. V. Grigorieva, A. A. Firsov, *Science* **2004**, *306*, 666.
[2] K. S. Novoselov, A. K. Geim, S. V. Morozov, D. Jiang, M. I. Katsnelson, I. V. Grigorieva, S. V. Dubonos, A. A. Firsov, *Nature* **2005**, *438*, 197.
[3] A. A. Balandin, S. Ghosh, W. Bao, I. Calizo, D. Teweldebrhan, F. Miao, C. N. Lau, *Nano Lett.* **2008**, *8*, 902.
[4] S. Stankovich, D. A. Dikin, G. H. B. Dommett, K. M. Kohlhaas, E. J. Zimney, E. A. Stach, R. D. Piner, S. T. Nguyen, R. S. Ruoff, *Nature* **2006**, *442*, 282.
[5] L. A. Ponomarenko, F. Schedin, M. I. Katsnelson, R. Yang, E. W. Hill, K. S. Novoselov, A. K. Geim, *Science* **2008**, *320*, 356.
[6] Z. Q. Yan, W. L. Yao, L. Hu, D. D. Liu, C. D. Wang, C. S. Lee, *Nanoscale* **2015**, *7*, 5563.
[7] X. H. Cao, Z. Y. Yin, H. Zhang, *Energy Environ. Sci.* **2014**, *7*, 1850.
[8] W. Lv, C. Zhang, Z. J. Li, Q. H. Yang, *J. Phys. Chem. Lett.* **2015**, *6*, 658.
[9] a) X. Xia, D. Chao, Z. Fan, C. Guan, X. Cao, H. Zhang, H. J. Fan, *Nano Lett.* **2014**, *14*, 1651; b) G. Zhu, Z. He, J. Chen, J. Zhao, X. Feng, Y. Ma, Q. Fan, L. Wang, W. Huang, *Nanoscale* **2014**, *6*, 1079.
[10] E. Singh, Z. Chen, F. Houshmand, W. Ren, Y. Peles, H.-M. Cheng, N. Koratkar, *Small* **2013**, *9*, 75.
[11] N. Li, Q. Zhang, S. Gao, Q. Song, R. Huang, L. Wang, L. Liu, J. Dai, M. Tang, G. Cheng, *Sci. Rep.* **2013**, *3*, 1604.
[12] Q. Song, Z. Jiang, N. Li, P. Liu, L. Liu, M. Tang, G. Cheng, *Biomaterials* **2014**, *35*, 6930.
[13] W. Li, S. Gao, L. Wu, S. Qiu, Y. Guo, X. Geng, M. Chen, S. Liao, C. Zhu, Y. Gong, M. Long, J. Xu, X. Wei, M. Sun, L. Liu, *Sci. Rep.* **2013**, *3*, 2125.
[14] a) X. H. Xia, D. L. Chao, Y. Q. Zhang, Z. X. Shen, H. J. Fan, *Nano Today* **2014**, *9*, 785; b) Q. L. Fang, Y. Shen, B. L. Chen, *Chem. Eng. J.* **2015**, *264*, 753.
[15] J. H. Park, D. H. Cho, Y. Moon, H. C. Shin, S. J. Ahn, S. K. Kwak, H. J. Shin, C. Lee, J. R. Ahn, *ACS Nano* **2014**, *8*, 11657.
[16] D. A. Dikin, S. Stankovich, E. J. Zimney, R. D. Piner, G. H. B. Dommett, G. Evmenenko, S. T. Nguyen, R. S. Ruoff, *Nature* **2007**, *448*, 457.
[17] S. H. Lee, H. W. Kim, J. O. Hwang, W. J. Lee, J. Kwon, C. W. Bielawski, R. S. Ruoff, S. O. Kim, *Angew. Chem. Int. Ed.* **2010**, *49*, 10084.
[18] H.-P. Cong, X.-C. Ren, P. Wang, S.-H. Yu, *Sci. Rep.* **2012**, *2*, 613.
[19] Z. P. Chen, W. C. Ren, L. B. Gao, B. L. Liu, S. F. Pei, H. M. Cheng, *Nat. Mater.* **2011**, *10*, 424.
[20] B. H. Min, D. W. Kim, K. H. Kim, H. O. Choi, S. W. Jang, H. T. Jung, *Carbon* **2014**, *80*, 446.
[21] B. Hsia, M. S. Kim, L. E. Luna, N. R. Mair, Y. Kim, C. Carraro, R. Maboudian, *ACS Appl. Mater. Int.* **2014**, *6*, 18413.
[22] D. D. Nguyen, S. Suzuki, S. Kato, B. D. To, C. C. Hsu, H. Murata, E. Rokuta, N. H. Tai, M. Yoshimura, *ACS Nano* **2015**, *9*, 3206.
[23] A. Reina, X. Jia, J. Ho, D. Nezich, H. Son, V. Bulovic, M. S. Dresselhaus, J. Kong, *Nano Lett.* **2009**, *9*, 30.
[24] Q. Yu, J. Lian, S. Siriponglert, H. Li, Y. P. Chen, S.-S. Pei, *Appl. Phys. Lett.* **2008**, *93*, 113103.
[25] S. J. Chae, F. Guenes, K. K. Kim, E. S. Kim, G. H. Han, S. M. Kim, H.-J. Shin, S.-M. Yoon, J.-Y. Choi, M. H. Park, C. W. Yang, D. Pribat, Y. H. Lee, *Adv. Mater.* **2009**, *21*, 2328.
[26] a) L. M. Malard, M. A. Pimenta, G. Dresselhaus, M. S. Dresselhaus, *Phys. Rep.* **2009**, *473*, 51; b) A. C. Ferrari, J. C. Meyer, V. Scardaci, C. Casiraghi, M. Lazzeri, F. Mauri, S. Piscanec, D. Jiang, K. S. Novoselov, S. Roth, A. K. Geim, *Phys. Rev. Lett.* **2006**, *97*, 187401.

[27] S. F. Zhao, Y. J. Gao, J. H. Li, G. P. Zhang, C. Y. Zhi, L. B. Deng, R. Sun, C. P. Wong, *ACS Appl. Mater. Inter.* **2015**, *7*, 6716.
[28] Y. He, W. Chen, X. Li, Z. Zhang, J. Fu, C. Zhao, E. Xie, *ACS Nano* **2013**, *7*, 174.
[29] T. W. Lin, C. S. Dai, K. C. Hung, *Sci. Rep.* **2014**, *4*, 10.
[30] W. W. Liu, C. X. Lu, X. L. Wang, K. Liang, B. K. Tay, *J. Mater. Chem. A* **2015**, *3*, 624.
[31] K. S. Kim, Y. Zhao, H. Jang, S. Y. Lee, J. M. Kim, K. S. Kim, J.-H. Ahn, P. Kim, J.-Y. Choi, B. H. Hong, *Nature* **2009**, *457*, 706.